

Direct numerical simulation of turbulent flows with cloud-like off-source heating

By A. J. BASU AND R. NARASIMHA

Jawaharlal Nehru Centre for Advanced Scientific Research, Jakkur Campus,
Bangalore 560064, India

(Received 10 September 1997 and in revised form 12 November 1998)

Direct numerical solutions of the incompressible Navier–Stokes equations have been obtained under the Boussinesq approximation for the temporal evolution of a turbulent jet-like flow subjected to off-source volumetric heating, of the kind that occurs in a cloud due to latent heat release on condensation of water vapour. The results show good qualitative agreement with available experimental data on spatially growing jets. Thus, heating accelerates the flow and arrests jet growth; and turbulence velocities increase with heating but not as rapidly as mean velocities, so normalized intensities drop. It is shown that the baroclinic torque resulting from the heating enhances the vorticity dramatically in all three directions, with a preferential amplification at the higher wavenumbers that results in a rich fine structure at later times in the evolution of the jet. Streamwise vortex pairs, rendered stronger by mean flow acceleration, appear to be responsible for large *expulsive* motions at certain transverse cross-sections in the ambient fluid near the heated flow; together with the disruption of the toroidal component of the coherent vorticity achieved by heating, this results in an entraining velocity field that is qualitatively different from that around unheated turbulent jets. This mechanism may provide a plausible explanation for the experimentally observed drop in entrainment with off-source heating.

1. Introduction

There are several reasons for undertaking a study of turbulent flows into which heat can be released volumetrically. For example, heat release occurs in combusting flows due to chemical reactions; several investigations of reacting flows, both experimental (Dimotakis 1991; Broadwell & Mungal 1991) and computational (involving direct numerical solution of the Navier–Stokes equations: see McMurtry *et al.* 1986; Mathew & Basu 1998), have been reported in recent years. In flows such as diffusion flames, entrainment and mixing lead to chemical reaction, which results in heat release, which in turn may affect both entrainment and mixing, i.e. the connections are tightly coupled, and cyclic. To understand the effect of heat release specifically on mixing, however, it is desirable to study a flow situation in which controlled amounts of heat can be injected into the flow, without any connection to chemical reaction. In particular, here we are interested in investigating flow situations where only negligible changes occur in density and transport parameters (such as viscosity) due to heating – thus considerably simplifying the equations governing the flow. Because of this simplification, the results obtained here, while not applicable in detail to combusting flows, are still believed to describe one mechanism that may be of importance to a

wide class of flows that occur in nature as well as technology, where the buoyancy force plays a significant role.

Such a flow situation has direct relevance to some geophysical problems, in particular the development of a cloud. Rising humid air in the atmosphere cools by adiabatic expansion, and the condensation of water vapour which occurs as a consequence above a certain height releases significant quantities of latent heat. This heat release could exert a strong influence on the flow. This situation acquires special interest because it has been realized experimentally (Elavarasan *et al.* 1995; Bhat & Narasimha 1996) by ohmic heating of a jet of electrically conducting liquid. These experiments provide data that can serve as a source of validation for the simulations that we shall report here, and we shall be able to study such key variables as vorticity which are hard to measure experimentally but are easily derived from numerical solutions. In the experiments a controlled amount of heat is injected volumetrically into the region between two selected streamwise stations in the far field of a spatially evolving jet. The results show that heating accelerates the flow and inhibits jet growth; for very large heating, growth may cease altogether or even become negative. Heating is also found to increase the turbulence velocities, but not as rapidly as the mean velocity, so normalized intensities drop. The inhibition of jet growth is such that there may be a reduction in overall entrainment for sufficiently large heat injection. There are also indications of disruption of structures in the flow. Rather similar observations have recently been reported for a plume subjected to off-source heating as well (Venkatakrishnan *et al.* 1998). As we shall see, the present simulations reproduce qualitatively many of the features seen in the laboratory experiments.

The jet flow with off-source volumetric heating should only be considered a ‘cartoon’ (in the sense of Corcos 1988) for the flow in a cloud, as has been explained in detail in Bhat & Narasimha (1996). A cloud is of course a complex flow, involving microphysics, thermodynamics, multiple phases, etc.; furthermore the amount of heat released itself depends on other thermal and fluid flow parameters of the cloud. It is not our objective to make a realistic simulation that fully accounts for all these factors. Instead we concentrate on the effects of heat release on the structure of the turbulence. For this purpose a satisfactory idealization is provided by the Boussinesq approximation, whose applicability to fluid-dynamical problems of the kind considered here has been established in various earlier studies (e.g. Turner 1973; Tritton 1988).

Several direct numerical simulations of the early stages of evolution of circular, unheated jet flow have been reported previously (e.g. Melander, Hussain & Basu 1991; Verzicco & Orlandi 1994; Chen, Lienau & Kollmann 1995). Our interest here, with a view to atmospheric application (where condensation levels are effectively in the far field of a rising plume), is in studying the effect of heat release when the flow has attained self-similarity. This becomes computationally expensive to handle in a spatial simulation, so we have adopted a temporal spectral solution technique. A code that has earlier been used extensively for studying (unheated) jets (Basu, Narasimha & Sinha 1992; Mathew & Basu 1997) has been modified for this purpose.

The plan of the paper is as follows. In §2, we describe the problem, the governing equations, and the initial and boundary conditions. In §3, the spectral method of solution used here is described in detail, along with issues concerning validation of the numerical scheme and the computer code. The results for the unheated jet are presented in §4, focusing especially on its similarity behaviour. In §5, we study the effects of heating on jet evolution: specifically examined are the effects of variation of the amount of heating, and different heat injection profiles. In §6

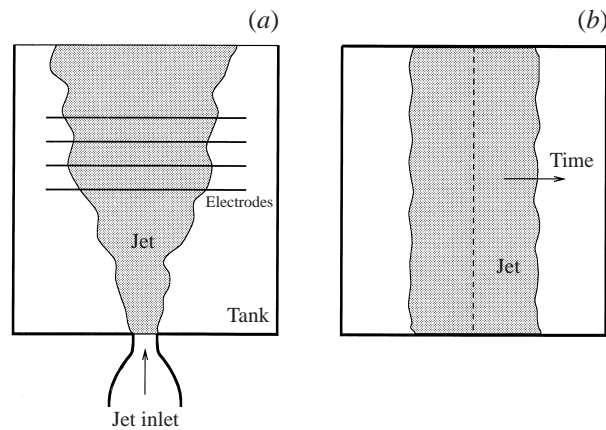


FIGURE 1. Schematics of (a) laboratory setup for a spatially developing jet, (b) the temporal simulation adopted in the present study.

and §7 respectively, we look at how heating alters the vorticity distribution and the entrainment characteristics in a jet. Finally, some conclusions are presented in §8.

2. Statement of the problem

The laboratory experiments mentioned above involve actual spatial development of a turbulent liquid jet issuing from a nozzle into a tank filled with the same liquid, along with volumetric heat addition over a certain streamwise distance after a self-similar state has been reached (see figure 1a). Computing such flows accurately, so that all the relevant length and time scales are captured, can be extremely demanding on both computer time and memory. Therefore, it was decided to compute a temporal analogue of the problem (figure 1b), where one studies the time-evolution of a cylindrical mixing layer inside a computational domain which is periodic in all the three space directions. After self-similarity is obtained in the computed mean velocity and turbulent stresses, heat is injected into the region occupied by the jet fluid, beginning at time t_{ho} . The heat-injection is switched off at time $t_{ho} + t_h$, where the duration of the heating t_h is typically of the order of one or more eddy-turnover times. Thus, while in the laboratory heat is injected at all times into a limited streamwise region along the jet, in the present temporal simulation we inject heat over a limited time duration into the entire flow.

The advantage of using a periodic domain is the ease with which spectral methods based on the fast Fourier transform (FFT) can be used to compute the flow reasonably fast and with high accuracy; the main drawback is that no rigorously quantitative comparison with the actual laboratory data can be made. It is important, however, to note that the periodic boundary conditions produce a flow that, while not identical with the spatially developing jet, nevertheless closely resembles it. Thus, although we capture three-dimensional structures of the kind known to occur in a laboratory jet, such events as ring formation and pairing now occur over the temporal evolution of the flow, and not in a particular region in space. The calculations are therefore not strictly representative of the evolution of either an axisymmetric jet or wake, but of a cylindrical (or tubular) mixing layer. Because of structural similarities with the early stages of a laboratory jet (see, for example, Liepmann & Gharib 1992), it should therefore be possible to form ideas about the laboratory flow from such a simulation.

In what follows, we will call the simulated flow a ‘jet’ for the sake of convenience. We return to this issue later in §4.3.

2.1. Governing equations

In the laboratory experiments mentioned above, as well as in the atmosphere, the flow may be considered to be nearly incompressible as the density changes due to heating are small. Furthermore, it can be assumed that temperature variations are introduced by some process independent of the flow dynamics. Since the Lagrangian acceleration of fluid particles in the jet is very small compared to the acceleration due to gravity \mathbf{g} , we can assume that the Boussinesq approximation is valid – that is, the effect of density changes in the flow (because of heating) appears only as a buoyancy term in the momentum equation, and does not significantly affect the inertial terms or the values of the transport parameters (see Turner 1973 for a critical discussion of this approximation). The heat injected into the flow appears as a source term in the energy equation, giving us the governing equations for the problem as

$$\nabla \cdot \mathbf{u} = 0, \quad (2.1)$$

$$\frac{\partial \mathbf{u}}{\partial t} + (\mathbf{u} \cdot \nabla) \mathbf{u} = -\frac{1}{\rho} \nabla p + \nu \nabla^2 \mathbf{u} - \mathbf{g} \alpha T, \quad (2.2)$$

$$\frac{\partial T}{\partial t} + (\mathbf{u} \cdot \nabla) T = \kappa \nabla^2 T + \frac{J}{\rho c_p}, \quad (2.3)$$

where \mathbf{u} is the velocity vector, ρ the density of the fluid, p the pressure, ν the kinematic viscosity of the fluid, α the coefficient of thermal expansion, T the change in temperature above ambient, κ the thermal diffusivity, J the rate of heat addition per unit volume, and c_p the specific heat at constant pressure.

While the acceleration due to gravity \mathbf{g} acts vertically downwards, in the present computations we use a Cartesian coordinate system whose z -axis is positive upwards. Therefore $\mathbf{g} = -g\mathbf{e}_z$, where \mathbf{e}_z is the unit vector along the positive z -direction. In the case of the unheated jet $T = 0$, and we need to solve the incompressible Navier–Stokes equations, which are essentially the equations (2.1) and (2.2), with the last (buoyancy) term omitted in the latter.

2.2. Non-dimensionalization

Equations (2.1)–(2.3) respectively express conservation of mass, momentum and energy. To non-dimensionalize these equations, we use the initial diameter d_0 and the initial centreline velocity U_0 of the cylindrical mixing layer, and a characteristic temperature difference T_0 (defined below) as scales. The nature of the continuity equation (2.1) does not change upon non-dimensionalization. Thus, using an asterisk for non-dimensional variables, we get

$$\nabla^* \cdot \mathbf{u}^* = 0. \quad (2.4)$$

Recalling that the heat is injected over the duration t_h into the flow, we define T_0 as the net temperature change that would result if the total heat Jt_h were injected uniformly over the unit volume: $T_0 = Jt_h/\rho c_p$. The non-dimensional energy equation (2.3) then becomes

$$\frac{\partial T^*}{\partial t^*} + (\mathbf{u}^* \cdot \nabla^*) T^* = \frac{1}{Re Pr} \nabla^{*2} T^* + H(t^*) \frac{d_0}{U_0 t_h} g(r^*), \quad (2.5)$$

where $Re = U_0 d_0 / \nu$ is the Reynolds number, $Pr = \nu / \kappa$ is the Prandtl number, and

$$\begin{aligned} H(t^*) &= 1 & \text{for } t_{h0}^* < t^* < t_{h0}^* + t_h^* \\ &= 0 & \text{otherwise,} \end{aligned}$$

and $g(r^*)$ is a prescribed function that determines the radial distribution of heat injected into the flow.

Similarly non-dimensionalizing the momentum equation (2.2), we get

$$\frac{\partial \mathbf{u}^*}{\partial t^*} + (\mathbf{u}^* \cdot \nabla^*) \mathbf{u}^* = -\nabla^* p^* + \frac{1}{Re} \nabla^{*2} \mathbf{u}^* + H'(t^*) G C_h T^* \mathbf{e}_z, \quad (2.6)$$

where

$$\begin{aligned} H'(t^*) &= 1 & \text{for } t^* \geq t_{h0}^*, \\ &= 0 & \text{for } t^* < t_{h0}^*, \end{aligned}$$

and

$$G \equiv \frac{\alpha g J d_h^2}{\rho c_p U_h^3} \quad (2.7)$$

is a non-dimensional heat release parameter; here d_h and U_h are respectively some appropriate length and velocity scales in the heat injection region (such as the local half-width and centreline velocity of the jet at the start of heat injection). The other non-dimensional parameter in (2.6) is

$$C_h \equiv \frac{U_h t_h d_0}{d_h} \left(\frac{U_h}{U_0} \right)^2, \quad (2.8)$$

whose value will remain constant during the present study. (This corresponds to fixing the spatial region over which heat is added in the laboratory jet.) Note that the parameter G used here is the strict analogue of that introduced by Bhat & Narasimha (1996), differing from their definition only because of the temporal nature of the present problem. It is rather like a bulk Richardson number, being a measure of the ratio of buoyancy to inertial forces.

Since G and C_h appear only as a product in equation (2.6), it is appropriate to introduce $G^* = G C_h$ as the relevant parameter governing heat release, and we will use G^* in place of G and C_h from now onwards.

The governing parameters for this flow are therefore Re , Pr and G^* , along with the duration t_h^* and distribution $g(r^*)$ of the heat injection term in the energy equation (2.5).

2.3. Initial and boundary conditions

The equations are solved here in a Cartesian coordinate system $\mathbf{x} = (x, y, z) = (x_1, x_2, x_3)$. However, in order to facilitate the description of initial conditions relevant to the (temporally-evolving) cylindrical mixing layer in question, we shall also use a cylindrical coordinate system (r, θ, z) such that $x = r \cos \theta$, $y = r \sin \theta$. The corresponding velocities are (u, v, w) and (u_r, u_θ, w) in the Cartesian and cylindrical systems respectively.

The initial conditions are chosen to simulate a flow that is similar (in a temporal sense) to that of a jet issuing from a round nozzle. Thus, we have a tubular shear layer along the vertical or z -direction at time $t = 0$. The streamwise or w -velocity has

a top-hat profile with a tan-hyperbolic shear layer:

$$\begin{aligned} w &= 1, & \forall r \leq r_0 - \delta/2 \\ &= 0, & \forall r \geq r_0 + \delta/2 \\ &= \frac{1}{2} \left(1 - \tanh \frac{r - r_0}{2\theta_0} \right), & \forall r_0 - \delta/2 < r < r_0 + \delta/2, \end{aligned} \quad (2.9)$$

where δ is the characteristic width of the shear layer. Here r_0 is the initial mean radius of the shear layer, θ_0 is the initial momentum thickness, and u_θ and u_r are assumed to be zero everywhere. We impose a small perturbation on this shear layer corresponding to an increment in u_r given by

$$\Delta u_r = f(r) \left[\sum_j a_j \sin \left(\frac{2\pi z}{\lambda_j} + \psi_j \right) + a_\theta \sum_l \sin(l\theta + s_l) \right], \quad (2.10)$$

with prescribed amplitudes a_j and a_θ , streamwise wavelength λ_j and phases ψ_j and s_l ; $f(r)$ is the filtering function

$$f(r) = \exp \left[-2 \left(\frac{r - r_0}{\delta} \right)^2 \right], \quad (2.11)$$

which helps to contain the initial perturbations within the shear layer.

Even though our focus in this study is primarily on the late times after the jet has developed self-similarity, we nevertheless compute through the instability and transition phases of the jet; this approach has been taken here because it is difficult to prescribe an ‘initial’ far-field condition that contains the representative vortical structures which are so essential to the points being made here. Specifying mean and fluctuating velocities as starting conditions in the far field (as is usually done) will not help the present simulations, since we are also interested in the structural details of the flow. For reasons already discussed, heat addition takes place only at later times when the computed mean velocity and Reynolds stresses have achieved self-similarity. The temperature everywhere is uniformly zero till the heat addition commences. The details of heat addition are discussed later in connection with the results in §5.

The boundary conditions are taken to be periodic in each space direction for all primary variables. (This facilitates the use of Fourier spectral schemes, and hence FFTs.) The size of the computational domain (one periodic cubical box of dimension $L \times L \times L$) is 4 times the diameter d_0 of the tubular shear layer at $t = 0$. Thus,

$$\left. \begin{aligned} \mathbf{u}(\mathbf{x}, t) &= \mathbf{u}(\mathbf{x} + L\mathbf{e}_i, t), & p(\mathbf{x}, t) &= p(\mathbf{x} + L\mathbf{e}_i, t), \\ T(\mathbf{x}, t) &= T(\mathbf{x} + L\mathbf{e}_i, t), & i &= 1, 2, 3. \end{aligned} \right\} \quad (2.12)$$

3. Method of solution

Equations (2.5)–(2.6) are solved along with the continuity equation (2.4) in a Cartesian coordinate system using the Fourier Galerkin (spectral) technique. The basic philosophy of the scheme is similar to that of Orszag (1971) for direct solution of the incompressible Navier–Stokes equations. No de-aliasing is used here, so the scheme may be considered to be ‘pseudospectral’.

We now drop the asterisk (except on G^*) for convenience and introduce the Fourier

expansions

$$\mathbf{u}(\mathbf{x}, t) = \sum_{\mathbf{k}' \leq K} \hat{\mathbf{u}}(\mathbf{k}', t) \exp\left(i \frac{2\pi}{L} \mathbf{k}' \cdot \mathbf{x}\right) \quad (3.1)$$

and similar ones for p and T ; here $\mathbf{k}' = (k'_x, k'_y, k'_z) = (k'_1, k'_2, k'_3)$ is an integer wave vector, $k'^2 = k'_\alpha k'_\alpha$ (using the summation convention), $K = N/2$ is a finite cut-off (N being the number of grid points along each direction), and $\mathbf{k}' \leq K$ means $-K \leq k'_\alpha \leq K$ for $\alpha = 1, 2, 3$. The quantities $\hat{\mathbf{u}}(\mathbf{k}', t)$, $\hat{p}(\mathbf{k}', t)$ and $\hat{T}(\mathbf{k}', t)$ are the Fourier-space (\mathbf{k}' -space) representations of the corresponding quantities. Using these expansions, and $\mathbf{k} = (2\pi/L)\mathbf{k}'$, we can rewrite the governing equations (2.4)–(2.6) in Fourier space as (with $\hat{\mathbf{u}}$, \hat{p} and \hat{T} being functions of (\mathbf{k}, t))

$$i\mathbf{k} \cdot \hat{\mathbf{u}} = 0, \quad (3.2)$$

$$\frac{\partial \hat{\mathbf{u}}}{\partial t} = -[(\mathbf{u}(\mathbf{x}, t) \cdot \nabla) \mathbf{u}(\mathbf{x}, t)]_{\mathbf{k}} - i\mathbf{k} \hat{p} - \frac{1}{Re} k^2 \hat{\mathbf{u}} + H'(t) G^* \hat{T} \mathbf{e}_z, \quad (3.3)$$

$$\frac{\partial \hat{T}}{\partial t} = -[(\mathbf{u}(\mathbf{x}, t) \cdot \nabla) T(\mathbf{x}, t)]_{\mathbf{k}} - \frac{1}{Re Pr} k^2 \hat{T} + H(t) \frac{d_0}{U_0 t_h} \hat{g}(r), \quad (3.4)$$

where the expressions within the square brackets are convolution sums to be evaluated in Fourier-space. Using the incompressibility condition (3.2), one can eliminate pressure from equation (3.3), and replace the first two terms on the right-hand side of (3.3) along any space direction α by (see Orszag 1971)

$$-\frac{i}{2} Q_{\alpha\beta\gamma}(\mathbf{k}) \sum_{\substack{\mathbf{m}+\mathbf{n}=\mathbf{k} \\ m, n \leq k}} u_\beta(\mathbf{m}, t) u_\gamma(\mathbf{n}, t), \quad (3.5)$$

where

$$Q_{\alpha\beta\gamma} = k_\beta(\delta_{\alpha\gamma} - k_\alpha k_\gamma / k^2) + k_\gamma(\delta_{\alpha\beta} - k_\alpha k_\beta / k^2), \quad (3.6)$$

and $\delta_{\alpha\beta}$ is the Kronecker-delta function.

Equations (3.2)–(3.4), with the modification given by (3.5), make up the governing equations in Fourier space. To compute the Fourier space convolution sums in these equations, the variables are first transformed to physical space by FFTs, the convolution sums obtained, and the results transformed back to Fourier space using FFTs. Such an approach is computationally efficient due to the high speed of executing FFTs. It can give rise to aliasing errors, but, as Canuto *et al.* (1988, p. 211) point out, accuracy considerations do not constitute a compelling reason to eliminate aliasing errors; we have therefore made no attempt here to dealias the computational results.

The periodic boundary conditions are automatically satisfied by choosing a Fourier spectral representation. For integrating in time, we use a third-order-accurate Runge–Kutta scheme to begin the computation, followed by a third-order-accurate Adams–Bashforth scheme to continue with the time-integration. Thus the computations can be restarted from any point in time at which data are stored.

3.1. Obtaining divergence-free initial conditions

The perturbations Δu_r given by (2.10), imposed at time $t = 0$, constitute a divergent velocity field $\mathbf{u}_d(\mathbf{x}, t = 0)$. We can, however, construct a divergence-free field using the Helmholtz decomposition

$$\mathbf{u}_d = \nabla \Phi + \nabla \times \Psi, \quad (3.7)$$

where Φ and Ψ are scalar and vector potentials, respectively. Since

$$\nabla \cdot \mathbf{u}_d = \nabla^2 \Phi = \epsilon, \quad (3.8)$$

say, we have in Fourier space $\hat{\Phi}(\mathbf{k}) = -\hat{\epsilon}(\mathbf{k})/k^2$ for $k \neq 0$; it follows that the divergence-free field is the inverse Fourier transform of

$$\hat{\mathbf{u}}(\mathbf{k}, 0) = \begin{cases} \hat{\mathbf{u}}_d(\mathbf{k}, 0) - (\mathbf{k} \cdot \hat{\mathbf{u}}_d)\mathbf{k}/k^2 & \text{for } k \neq 0 \\ 0 & \text{for } k = 0. \end{cases}$$

3.2. Validation

Beyond $t = 0$ the incompressibility constraint is not explicitly implemented into the formulation or the computer code. Thus, one can expect the value of maximum divergence in the computational domain to provide a measure of solution accuracy. In the present calculations, the maximum divergence anywhere in the field stays bounded to values very close to the truncation errors even at the end of the computations. This is direct evidence that the incompressibility constraint is accurately satisfied, and indirect evidence that the incompressible Navier–Stokes equations are being computed correctly.

It is unnecessary to provide further evidence here on the validation, since the basic formulation is quite well-established (see Orszag 1971), and the present code has been validated by extensive computations earlier (e.g. Basu *et al.* 1992; Mathew & Basu 1997).

As the temperature differential T in the present problem arises from heat addition, it must be essentially positive. However, small errors in computation that may result in pockets of small negative temperature can accumulate over time into disastrous effects in the nonlinear calculations made here since temperature is an active scalar, and influences the flow directly (unlike passive scalars like dye concentration). To maintain positivity of temperature, we follow a simple procedure used by Riley, Metcalfe & Orszag (1986), which merely involves setting to zero at every time step any small negative temperature that may arise. It has been shown by Riley *et al.* that using this simple filter one is still able to get superalgebraic convergence.

In all the computations reported here (for both heated and unheated jet), we have maintained a constant Reynolds number $Re = 1600$ based on quantities at time $t = 0$; this Reynolds number is within the range (1360–3200) studied by Elavarasan *et al.* (1995). Computations are carried out using both 64^3 and 128^3 grids. The results presented in §4 contain data from simulations using both these grids, whereas in §5 only the 64^3 grid results are used. Finally in §6 and §7, where the physical and structural details of vorticity are analysed, the 128^3 grid is employed. The time steps used for computations are $\Delta t = 0.005$ for the 64^3 grid, and $\Delta t = 0.0025$ for the 128^3 grid. In the heated cases, the corresponding time step is halved to resolve the smaller scales that are found to be generated in the flow by heat addition. The time steps chosen here for computing the evolution of either the unheated or the heated jet are less than those required for numerical stability, as confirmed by trial simulations using different time steps.

The computations have been carried out on an R10000-based 4-processor Silicon Graphics Power Challenge computer. The CPU time required per step for the 64^3 calculations is about 1 s, whereas for the 128^3 grid it is about 9 s. Computations have been carried out up to a non-dimensional time of $t = 40$. Beyond this time the jet begins to fill the computational box, and thus nearby (periodic) boxes can affect the subsequent evolution.

We have used a certain default initial condition for all results presented here, except in §4.2 where the effects of different initial conditions will be studied. In this default condition, which we shall call Case I, we use three streamwise modes with wavelengths $\lambda_1 = L$, $\lambda_2 = L/2$, and $\lambda_4 = L/4$ (see (2.10)); the amplitudes of these modes are $a_1 = 0.01$, $a_2 = 0.02$ and $a_4 = 0.03$, and the phases are identically zero. Along the azimuthal direction we have 16 modes with equal amplitudes $a_\theta = 0.003$ and random phases generated by a pseudo-random number generator. The initial width δ of the shear layer is $L/16$.

4. The unheated jet

We begin presentation of our results with those for the temporal evolution of the unheated jet.

The initial temporal development of the unheated flow has been described elsewhere (Basu *et al.* 1992; Mathew & Basu 1997), and will not be considered in detail here. To summarize briefly, the development proceeds through the evolution of ring-like structures in the flow in the early stages of computation (up to about non-dimensional time $t = 5$). By $t = 10$, pairing takes place forced by the subharmonic perturbation that had been initially put in. Around $t = 15$, strong streamwise structures are seen in the flow and the ring structures develop strong azimuthal instabilities. By about $t = 20$, the rings apparently break down and very fine scales emerge. At later times, the entire flow field is filled with intermediate-scale structures with a marked streamwise orientation. As will be shown later, the flow achieves self-similarity in computed profiles of mean streamwise velocity and turbulence intensity by the time $t = 20$.

4.1. New integral scales

To obtain the radial profiles of mean streamwise velocity, turbulence intensity, etc., we first superimpose a cylindrical grid on top of the existing Cartesian grid. The values of different variables at the cylindrical grid points are then obtained via simple bilinear interpolation using the Cartesian grid values. Mean radial profiles are computed by averaging along both azimuthal and streamwise directions. (Averaging along the streamwise direction is consistent with the spirit of temporal simulation.) In experiments, it is usual to take the centreline velocity at any streamwise location as the local characteristic velocity, and the ‘half-width’ (where the mean streamwise velocity falls to half of the value at the centreline) as the local length scale. These quantities cannot be accurately estimated near the jet axis in the present simulations, because at the axis the number of data points for obtaining averages is too small, being limited to the number of grid points along the streamwise direction (64 or 128 in the present case). (Note, however, that the computed statistics improve with increasing r , as one can average over azimuthal points as well.) Indeed, it was this drawback that resulted in the unduly large variations (with time) of the computed centreline velocity and half-width in the previous calculations of Narasimha & Basu (1995). Thus, we need new characteristic local quantities that can be estimated more accurately.

A more fundamental point is that the invariants in the temporal jet are different from those in the spatial jet, and hence the appropriate length and velocity scales will also be different. Thus, in a temporal simulation subject to periodic boundary conditions, the mass flux in the flow (integrated over the computational domain) remains constant in time, but the momentum flux drops. We propose that the appropriate velocity and length scales in the present case (using $\bar{u}(r, t)$ for the mean

velocity) are therefore

$$\tilde{u}(t) = \frac{\int \bar{u}^2 r \, dr}{\int \bar{u} r \, dr}, \quad \tilde{b}(t) = \frac{\int \bar{u} r \, dr}{\left[\int \bar{u}^2 r \, dr \right]^{1/2}}. \quad (4.1)$$

These new scales can be quite accurately estimated, and incidentally overcome the drawback of the conventional local scales in the present simulations.

We can similarly define a new characteristic *integral* turbulence intensity $\tilde{u}'(t)$, defined in the same way as $\tilde{u}(t)$ except that u is replaced by the velocity fluctuations u' ; $\tilde{u}'(t)$ serves a function similar to that of the centreline turbulence intensity in experimental data.

4.2. Effect of initial conditions

It is necessary to investigate briefly whether the results presented here depend on the actual initial conditions used in the simulation. For this reason, we performed four simulations using both 64^3 and 128^3 grids and three different initial conditions, including Case I already defined in §3.2. For the second initial condition (Case II), we reduce a_θ to 0.0015, and use a different set of random phases generated using a different seed for the pseudo-random number generator. Finally, in Case III, we maintain a_θ the same as in Case I, but change the amplitudes of the three streamwise modes to $a_1 = 0.005$, $a_2 = 0.01$ and $a_4 = 0.015$ respectively; we also use different phases given by $\psi_1 = 0$, $\psi_2 = 0.5d_0$ and $\psi_4 = 0.25d_0$ respectively. The four simulations performed are: (i) 128^3 grid, initial conditions given by Case I, (ii) 64^3 grid, Case I, (iii) 64^3 grid, Case II, and (iv) 64^3 grid, Case III. In all these cases, we compute the evolution of the shear layers up to $t = 40$.

Figures 2(a) and 2(b) show the temporal evolution of \tilde{b} and \tilde{u} respectively for the different cases mentioned above. The velocity scale \tilde{u} appears to be insensitive to the nature of the initial perturbations, but the width \tilde{b} is less so. For the purpose of the present simulations, we can assume that such dependences do not alter the basic qualitative nature of the flows we compute. We will, nevertheless, investigate the issues concerning different initial conditions on the evolution of circular jets at a later time.

4.3. Similarity

As discussed previously in §2, the present temporal simulation cannot be unambiguously identified with any particular shear flow like a jet or wake. We can, however, use the well-known similarity arguments familiar in turbulent flow (e.g. Townsend 1976; Narasimha 1990) to seek appropriate asymptotic solutions for the temporal simulation. From the 'Reynolds number similarity principle' we can rule out viscosity as a relevant parameter. From dimensional arguments the only quantity involving the local scales \tilde{u}, \tilde{b} that has the dimensions of time is \tilde{b}/\tilde{u} , so it follows that $\tilde{b} = c\tilde{u}t$, where c is a constant. If further the mass flow is an invariant because of the periodic boundary conditions adopted in the simulation, it follows that $\tilde{b}^2\tilde{u}$ is a constant independent of time, say M . We then have the similarity laws for the temporal simulation,

$$\tilde{b} = (Mc)^{1/3} t^{1/3}, \quad \tilde{u} = (M/c^2)^{1/3} t^{-2/3}. \quad (4.2)$$

These laws imply that a characteristic local Reynolds number (proportional to $\tilde{b}\tilde{u}$) varies like $t^{-1/3}$; in this respect the flow considered resembles an axisymmetric wake.

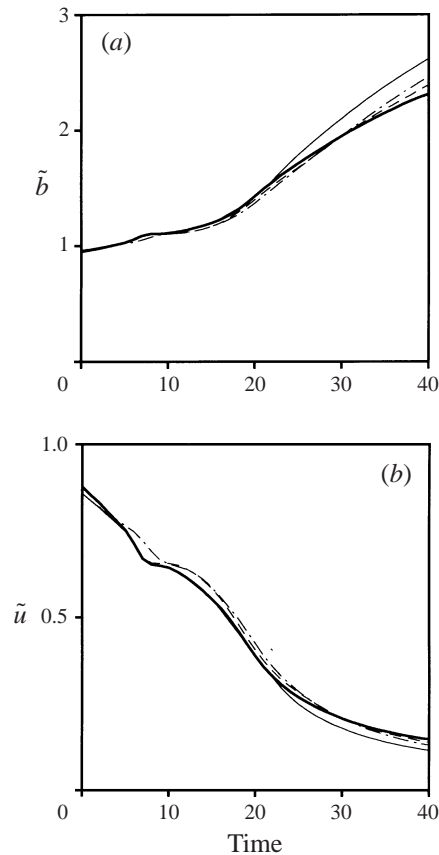


FIGURE 2. Effect of different initial conditions in the development of the jet. (a) Variation of jet width \tilde{b} with time for the different initial conditions (see text for details). (b) Variation of velocity scale \tilde{u} with respect to time for the same cases. —, 128^3 , Case I; —, 64^3 , Case I; - - - - -, 64^3 , Case II; - · - · -, 64^3 , Case III.

Thus the flow simulated here starts out like a jet developing from a cylindrical shear layer and ends up like a wake. Note that, as has been argued in the case of the axisymmetric wake, the continuous drop in the Reynolds number should eventually lead to laminarization; this would be an instance of what Narasimha & Sreenivasan (1979) have called dissipative reversion, which is generally very slow. In the present simulations, the local Reynolds number is seen to drop by about a third between $t = 20$ and 40, i.e. it still remains higher than 10^3 at the end of the simulation; so we may safely assume that laminarization is still far in the future indeed, and that the results to be discussed are representative of turbulent flow.

The simulation using the 128^3 grid, and initial conditions given by Case I, is taken here as the base-line to demonstrate similarity in the radial profiles of mean streamwise velocity and turbulence intensity. In figure 3(a) are plotted (to different scales) the integral measure of jet width \tilde{b}^3 , the local velocity scale $\tilde{u}^{-3/2}$, and the normalized integral turbulence intensity \tilde{u}'/\tilde{u} . As can be seen, from about $t = 20$, both \tilde{b}^3 and $\tilde{u}^{-3/2}$ show nearly linear growth, as predicted by the similarity arguments presented above. The normalized integral turbulence intensity shows a roughly linear growth (if one ignores the fluctuations) up to almost $t = 20$ or so, beyond which

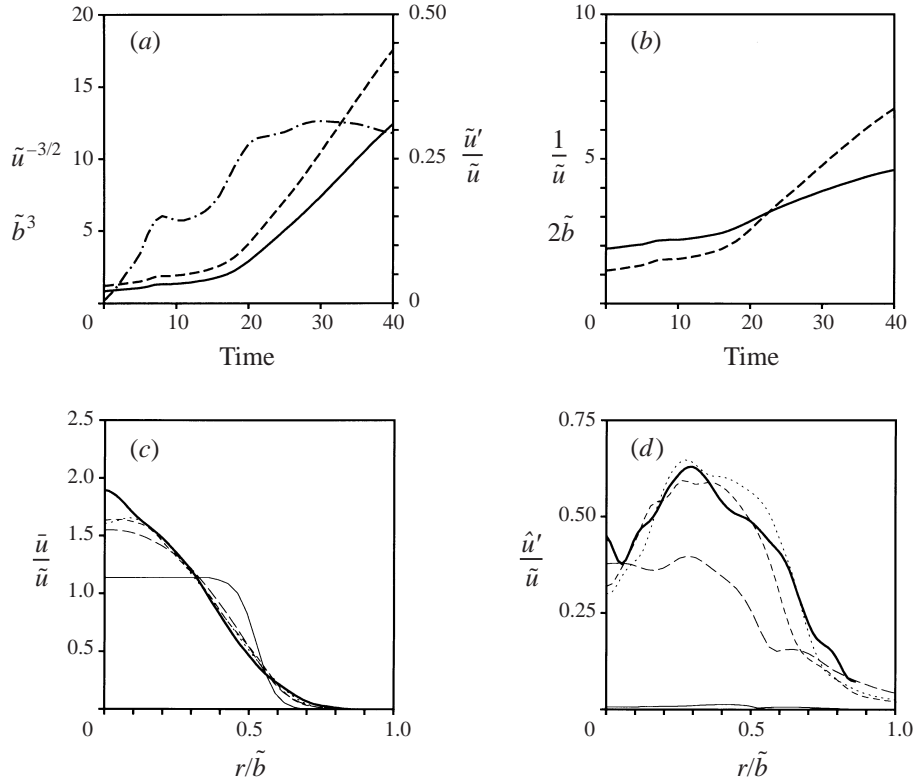


FIGURE 3. Evolution of computed length and velocity scales with time, to illustrate approach to self-similarity. (a) present scaling: —, \tilde{b}^3 ; - - - - , $\tilde{u}^{-3/2}$; - · - · - , $\tilde{u}'/\tilde{u}(t)$; (b) classical jet scaling: —, $2\tilde{b}$; - - - - , \tilde{u}^{-1} . (c, d) Convergence history of computed similarity profiles of \bar{u} (c) and \hat{u}' (d). The profile at $t = 0$ is shown by a *thin* solid line, and that at $t = 40$ by a *thick* solid line. Profiles between times $t = 10$ and $t = 30$ (at intervals of 10 time units) are shown by dashed curves with diminishing intervals (longest dashes for $t = 10$, shortest dashes for $t = 30$).

it appears to tend towards some constant value. For reasons already stated, it is not possible to compare the values of the different quantities described here with experimental data. Note, however, that the similarity behaviour described here is not locally very different from that of a turbulent jet over the later part of the duration over which the present flow is computed. As can be seen in figure 3(b), which shows the growth of \tilde{b} and $1/\tilde{u}$ with time, the behaviour during $t = 20$ to $t = 40$ does not show any dramatic departures from linearity; qualitative comparison with laboratory jets in the far field is therefore not unjustified.

Figure 3(c, d) shows the evolution of similarity profiles of mean streamwise velocity $\bar{u}(r, t)$ and the r.m.s. of the fluctuating streamwise velocity $\hat{u}'(r, t)$ respectively, both normalized by the local velocity scale $\tilde{u}(t)$; the radial distance is normalized by $\tilde{b}(t)$. The evolution is shown between time $t = 0$ and $t = 40$ at intervals of 10 non-dimensional time units. It can be clearly seen that the profiles of both the normalized mean streamwise velocity \bar{u}/\tilde{u} , and the normalized turbulence intensity \hat{u}'/\tilde{u} attain self-similarity within $t = 20$. The \bar{u} profile appears to be still evolving near the axis even though in general it looks similar to the usual Gaussian profiles seen in experiments. This behaviour is likely to be due to the fact that, as mentioned before, near the axis there are not enough computational data points to obtain meaningful statistics. The qualitative nature of the \hat{u}'/\tilde{u} profile looks reasonably similar to laboratory results.

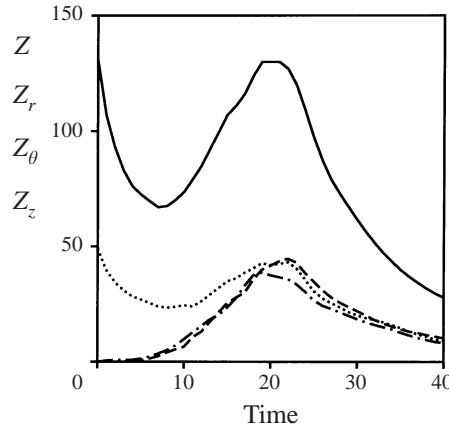


FIGURE 4. Computed evolution of enstrophy in the unheated jet: —, total enstrophy Z ; ·····, Z_θ ; - - - -, Z_z ; - · - · -, Z_r .

It is clear from the above discussion that the computed flow shows several basic qualitative characteristics of a turbulent jet.

4.4. Evolution of enstrophy

The enstrophy

$$Z = \int \int \int \|\boldsymbol{\omega}\|^2 r \, dr \, d\theta \, dz = Z_r + Z_\theta + Z_z \quad (4.3)$$

is an integral parameter describing the vorticity content in a flow; here $\|\boldsymbol{\omega}\|$ is the magnitude of the vorticity vector $\boldsymbol{\omega}$ (thus $\|\boldsymbol{\omega}\| = (\omega_r^2 + \omega_\theta^2 + \omega_z^2)^{1/2}$), and Z_r , Z_θ and Z_z are respectively the enstrophies of the components of vorticity along the r -, θ - and z -directions. The computed time evolution of all four quantities from the 128^3 simulation is shown in figure 4. The total enstrophy decreases while the roll-up process is in progress (up to about $t = 7$), beyond which the formation of streamwise vortices and vortex-stretching raises the total enstrophy till about $t = 20$; thereafter it decays monotonically. If we look at the component enstrophies, one can see that at $t = 0$ nearly all of the vorticity is azimuthal (as set by the initial conditions). Between $t = 5$ and $t = 20$ there is a consistent rise in the radial and streamwise enstrophies, while the azimuthal component shows an initial dip and subsequent rise. What is rather interesting is how, beyond the breakdown of the ring structures around $t = 20$, the component enstrophies tend towards similar values, while decreasing monotonically all the time. This points to strong inter-component transfer during the fully turbulent phase of the flow (beyond $t = 20$), leading to some kind of equipartition in the enstrophy, with vortical structures of different kinds in different directions.

5. The heated jet

Having shown the qualitative similarity of the computed unheated jet with the observed behaviour of turbulent jets in the laboratory, we now proceed to look at the effect of volumetric heat addition on the growth of such a jet. As shown before, the main parameters that affect the jet growth are Re , Pr , G^* and $g(r)$, the actual heating profile used. We will, for the 64^3 computations presented in this section, adopt the values $Re = 1600$ and $Pr = 7$ (for water at 20°C). Heat is added to the flow only

between the non-dimensional times $t = 32$ (after the flow achieves self-similarity) and $t = 34$, after which no further heat addition takes place. The flow evolution is, however, computed beyond heat addition up to $t = 40$. Since we will be looking mostly at computed *statistics* in the present section and not the details of the flow structure, the 64^3 grid is considered sufficient for the purpose.

We perform two sets of numerical experiments here. In the first set, the heat injection profile $g(r)$ is kept fixed, similar to that of the streamwise velocity at time $t = 32$, but the parameter G^* is assigned the values 0.01, 0.04 and 0.1 to examine the effects of change in total quantity of heat injected (the value of C_h in all these cases is 4.3×10^{-4}). Note that the heat addition here is axisymmetric, even though the computed jet is instantaneously non-axisymmetric at all times.

The second set of numerical experiments involves changing the actual heating profile $g(r)$ while keeping G^* fixed at 0.04. We use three different heating profiles that are similar to the computed mean streamwise velocity profiles in the unheated jet at times $t = 20, 32$ and 40 respectively. Care has been taken to scale each profile correctly so that the total amount of heat injected in all the three cases remains the same. At this point, it is important to note certain differences in the present computations when compared to the experiments of Bhat & Narasimha (1996). First, the parameter G (not G^*) in our computations is analogous (but not directly relatable) to the heat release number used to analyse the laboratory data. This is because of difficulties in establishing quantitative connections between the spatial extent of the heat-injection zone in the experiments and the duration of heat addition in the present computations. Second, heat addition in the experiments being due to ohmic losses in an electrically conducting fluid, the instantaneous distribution of heating imparted to the fluid is unlikely to be as smooth as the near-Gaussian axisymmetric heating profile used here; in principle the distribution in the experiments varies both in time and in space. However, in both cases there is a bulk addition of volumetric heating to the flow over a few eddy-turnover times, and it is this effect that we wish to study.

We now describe the results of these numerical experiments.

5.1. Effects of variation in G^*

In figure 5(a,b) we show the evolution with time (between $t = 25$ and $t = 40$) of \tilde{b}^3 and $\tilde{u}^{-3/2}$ respectively for the unheated jet, along with the effects of variation in G^* . When G^* is increased, the jet width (in terms of \tilde{b}) falls, and \tilde{u} increases, as has been reported by Elavarasan *et al.* (1995) and Bhat & Narasimha (1996). Figure 5(c,d) shows the integral turbulence intensity \tilde{u}' , respectively non-normalized and normalized by \tilde{u} . We see that as G^* increases, the actual \tilde{u}' increases but its ratio to \tilde{u} falls; i.e. \tilde{u}' does not increase as rapidly as \tilde{u} does. These results are again consistent with the experimental findings: Bhat & Narasimha (1996) report (see their figure 9b and the discussion in §4.3) that while the turbulence intensity u' may even double with sufficient heating, the normalized value can drop by about 35%; in the present simulations the normalized \tilde{u}' has fallen in some cases to about half its unheated value.

Figure 5(e,f) shows the profiles of mean streamwise velocity \bar{u} and the r.m.s. of the fluctuating streamwise velocity \hat{u}' in similarity variables at time $t = 40$, the end of our computation. Even with large G^* , one can see that the similarity in mean streamwise velocity is not lost. The small differences near the axis of the jet are likely to be related to the small size of samples there, as mentioned before. Figure 5(f) shows very clearly the fall in relative turbulence intensity as one increases G^* .

It must be stressed here that the behaviour of all the computed quantities $\tilde{b}^3, \tilde{u}^{-3/2}$

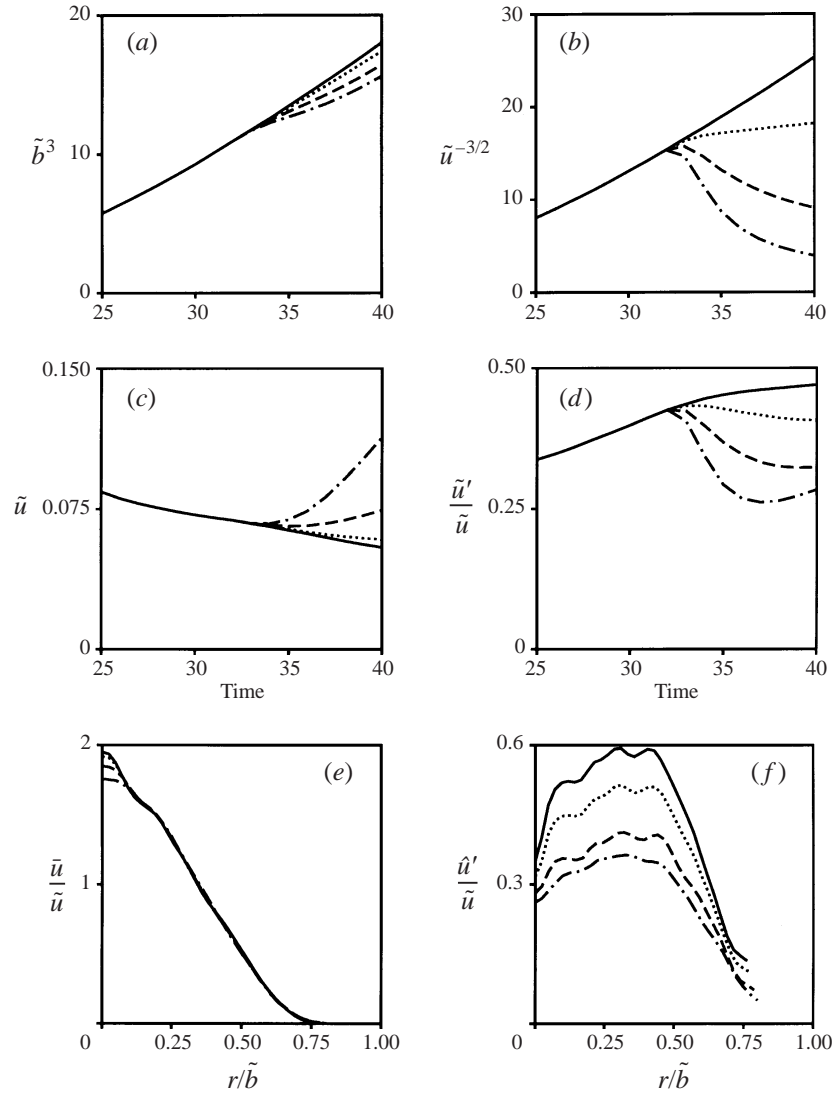


FIGURE 5. Effect of variation of heat release parameter G^* on the time evolution of: (a) \tilde{b}^3 , (b) $\tilde{u}^{-3/2}$, (c) \tilde{u}' , (d) \tilde{u}'/\tilde{u} , and on the similarity profiles at time $t = 40$ of: (e) mean streamwise velocity \tilde{u} , (f) r.m.s. of the fluctuating streamwise velocity \tilde{u}' . —, $G^* = 0$ (unheated); ·····, $G^* = 0.01$; ---, $G^* = 0.04$; - · - · -, $G^* = 0.1$.

and \tilde{u}' seen here is remarkably consistent with that seen for the corresponding relevant quantities (half-width, centreline mean streamwise velocity and centreline turbulence intensity) in the available experimental data (cf. figure 9, Bhat & Narasimha 1996). Even the rise in normalized \tilde{u}' at late times for high values of G^* is similar to that seen for normalized centreline turbulence intensity at large distances in the experiments. This greatly enhances our confidence in the relevance of the present computations to understanding the effect of heat addition in turbulent flows.

Figure 6(a–d) shows the distribution of vorticity magnitude $\|\boldsymbol{\omega}\|$ in the (y, z) -plane (passing through the axis of the jet) at $t = 40$ for $G^* = 0$ (unheated), 0.01, 0.04 and 0.1 respectively. For low values of G^* there is not much change in vorticity distribution,

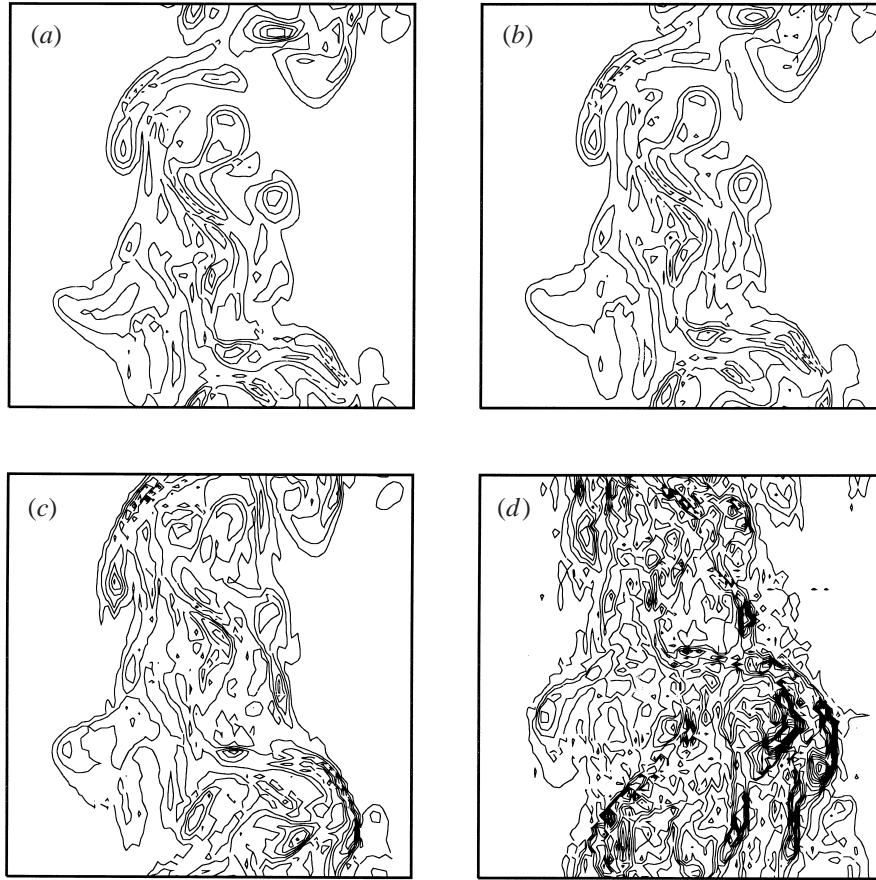


FIGURE 6. Effect of variation of heat release parameter G^* on the distribution of vorticity magnitude $\|\omega\|$ over the (y, z) -plane passing through the axis of the jet at $t = 40$: (a) $G^* = 0$, (b) $G^* = 0.01$, (c) $G^* = 0.04$, (d) $G^* = 0.1$. The contour levels are drawn at intervals of 0.5 starting from 0.5.

except that the entire field is advected slightly faster. But at larger G^* we begin to see the emergence of small-scale structures and an increase in the strength of the vorticity, presumably brought about by larger gradients in temperature, as we shall examine in more detail in §6 below.

5.2. Effect of changes in heat injection profile

The three different heat injection profiles used here, similar to the mean streamwise velocity profiles at times $t = 20, 32$ and 40 , will be called ‘narrow’, ‘moderate’ and ‘wide’ respectively. In all cases, $Re = 1600$, $G^* = 0.04$, and the heating profiles are scaled to achieve equal amount of total heat injection. Figure 7(a) shows that these heating profiles can alter the growth rate of the jet. A narrow profile decreases the growth rate, whereas a wide profile enhances it.

Figure 7(b) shows that \tilde{u} , on the other hand, is not related to the heat injection profile, but to the parameter G^* or the total amount of heat injected (which was kept constant in this case).

Figure 7(c, d) shows that the narrow heating profile causes more intense velocity fluctuations. It is important to note, however, that the fall in normalized integral turbulence intensity appears to be of the same order in all three cases. Interestingly,

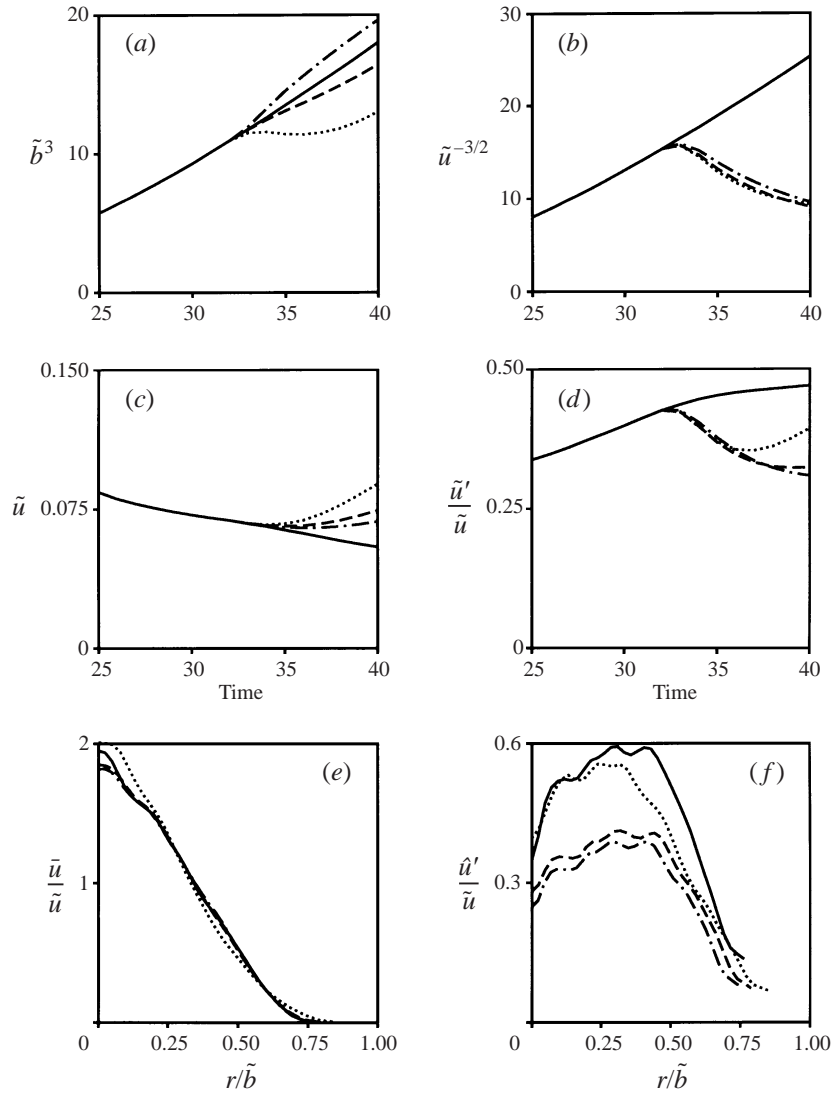


FIGURE 7. Effect of heating profile on the time evolution of (a) \tilde{b}^3 , (b) $\tilde{u}^{-3/2}$, (c) \tilde{u}' , (d) \tilde{u}'/\tilde{u} , and on the similarity profiles at time $t = 40$ of (e) mean streamwise velocity \tilde{u} , (f) r.m.s. of the fluctuating streamwise velocity \tilde{u}' : —, unheated jet; ·····, narrow heating profile; - - - -, moderate heating profile; - · - · -, wide heating profile.

the integral turbulence intensity for the narrow heating profile (figure 7d) picks up after the heat injection is stopped (beyond $t = 34$), exactly as in the experimental data for centreline turbulence intensity (see figure 9 of Bhat & Narasimha 1996). This behaviour is related to the large temperature gradients caused by the narrow heating profile; the temperature gradients continue to work at producing small-scale vorticity fluctuations even after heat injection is stopped, as we shall discuss in more detail in the next section.

Finally, figure 7(e, f) shows the profiles of the streamwise mean velocity \tilde{u} and the r.m.s. of the fluctuating streamwise velocity \tilde{u}' in similarity variables at time $t = 40$ for different heat injection profiles. As we can see, the mean velocity profiles maintain

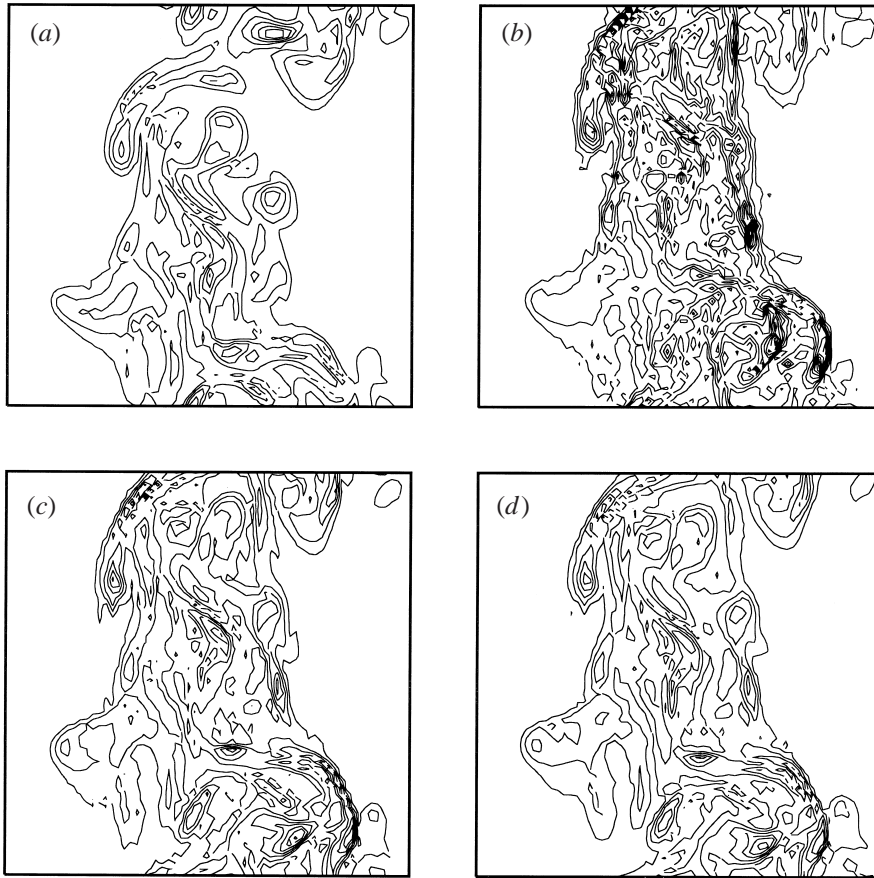


FIGURE 8. Effect of variation of heat injection profile on the distribution of vorticity magnitude $\|\omega\|$ over the (y, z) -plane passing through the axis of the jet at $t = 40$: (a) unheated jet, and different heating profiles: (b) narrow, (c) moderate, (d) wide. The contour levels are drawn at intervals of 0.5 starting from 0.5.

similarity to a large extent. Suppression in (normalized) \hat{u}' occurs only for moderate and wide heating profiles, whereas for the narrow heating profile \hat{u}' again picks up at later times and its radial distribution at time $t = 40$ is close to that of the unheated jet.

Examining the evolution of the flow quantities displayed in figures 5 and 7, one question that arises is whether an integral method can explain the results of the simulations. This question was considered by Bhat & Narasimha (1996) with regard to their experiments. To close the integral equations of mass, momentum and energy conservation, one needs to make a suitable entrainment assumption. Bhat & Narasimha show that the usual assumption of constant entrainment coefficient yields results that do not agree with observation. They attribute this failure to the structural changes taking place in the flow; at any rate it is clear that the development of more successful integral models for flows with heat addition of the type considered here demands the formulation of new hypotheses for entrainment. Such a study is outside the scope of the present paper, and so will not be considered here.

Figure 8(a–d) shows the distributions of vorticity magnitude $\|\omega\|$ resulting from different heat injection profiles. Production of small-scale vorticity is most marked

with the narrow heating profile, as already suggested by the turbulence intensity profiles described before, but with all three heating profiles it is clear that vorticity levels have gone up dramatically. The low-vorticity regions seen in figure 8(a) are filled up with heating, the ‘edges’ of the flow look much less convoluted, and the engulfment of ambient irrotational fluid seems very much weaker.

All of these features are in agreement with observations: thus, heating produces dramatic changes in the development of the mean parameters and the vorticity field in the jet.

6. Effect of heating on vorticity

The present simulations show that heating exerts a dramatic influence on the vorticity field. In order to examine in detail this effect, which appears to hold the key to understanding the effect of heating on the turbulence, we look specifically at two simulations based on the 128^3 grid. One is the usual unheated jet whose evolution, starting with the initial condition described previously as Case I, has been computed up to non-dimensional time $t = 40$. In the other case, heat is applied between the times $t = 25$ and $t = 32$ and the flow evolution is computed up to $t = 35$. The relevant parameters for the computations are $Re = 1600$, $Pr = 7$, $G^* = 0.04$. The time step used for computing the evolution of the unheated jet is $\Delta t = 0.0025$, whereas for the heated jet it has been reduced to $\Delta t = 0.00125$; both values are within the restrictions imposed by stability considerations, as discussed before.

To appreciate how heating affects vorticity, we first derive the equations governing the vorticity in the present flow.

6.1. The vorticity equations

Taking the curl of equation (2.2), we obtain

$$\frac{\partial \boldsymbol{\omega}}{\partial t} + (\mathbf{u} \cdot \nabla) \boldsymbol{\omega} - (\boldsymbol{\omega} \cdot \nabla) \mathbf{u} - \nu \nabla^2 \boldsymbol{\omega} = \alpha \mathbf{g} \times \nabla T, \quad (6.1)$$

where the terms on the left are familiar from classical, incompressible flow theory. The term on the right is a source of vorticity; it arises from the baroclinic torque $\nabla p \times \nabla \rho$ when the pressure gradient ∇p is replaced by its value in the hydrostatic approximation, and the density gradient $\nabla \rho$ by the temperature gradient, to which it is proportional in the approximation we are using.

Note that although gravity is a conservative force, vorticity can be created under the Boussinesq approximation. As the acceleration \mathbf{g} acts vertically, it is clear from (6.1) that only the horizontal gradients of temperature are relevant, and only the horizontal components of the vorticity (comprising ω_r and ω_θ) are directly affected. It is easily verified (see figure 9) that if the (mean) temperature drops radially outward (as it does in the heated jet), the initial mean azimuthal vorticity is enhanced due to the heating, i.e. the shear in the jet increases.

By decomposing the vorticity into a mean $\bar{\boldsymbol{\omega}}$ and a fluctuation $\boldsymbol{\omega}'$, we can use standard methods to derive equations for each of them. It is easily seen that the mean baroclinic generation terms are

$$\frac{\alpha g}{r} \frac{\partial \bar{T}}{\partial \theta}, \quad -\alpha g \frac{\partial \bar{T}}{\partial r}, \quad 0$$

for $\bar{\omega}_r$, $\bar{\omega}_\theta$ and $\bar{\omega}_z$ respectively.

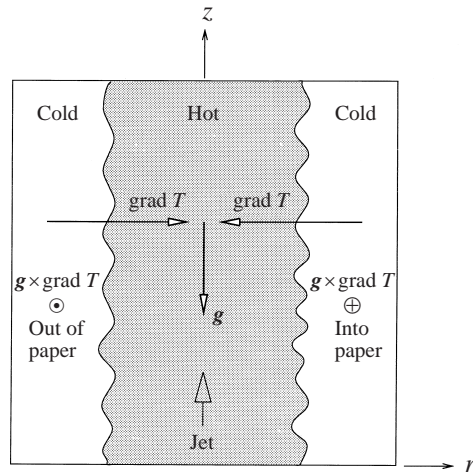


FIGURE 9. Schematic of the jet and the heating showing the direction of the baroclinic torque. As the jet is hottest near the axis, temperature falls away on either side, leading to the vectors ∇T and $\mathbf{g} \times \nabla T$ having the directions shown, on either side of the axis.

6.2. Vorticity components

The effect of heating on the azimuthal, streamwise and radial components of the vorticity field is shown in figure 10. The vorticity distributions at the same non-dimensional time $t = 35$ are plotted side-by-side for the unheated and heated case for each component. The positive-valued contours are shown using solid lines, whereas the negative-valued ones are in dotted lines. For the azimuthal and radial components, there is an apparent abrupt change of sign at the axis, but this is a consequence of the definition of sign in the cylindrical coordinate system. The Cartesian components of the vorticity do not change sign across the centreline; the implication is that there is no toroidal or radial organization of the vorticity near the axis, especially in the heated jet.

From figure 10(b,d,f) we see that the nearly irrotational regions evident within the unheated jet (figure 10(a,c,e)) are filled with strong vorticity due to heating. Furthermore, there is considerable fine-scale vortical activity, and the 'edges' of the flow are less convoluted. All of these features are completely consistent with the experimental findings. What is perhaps remarkable is that all three components of vorticity increase dramatically. In general, the vorticity field with heating appears to possess much less organization than the unheated flow.

At this stage it is necessary to discuss the role of coherent structures in the flow. Experimentally these have often been inferred on the basis of flow visualization with passive tracers, but the availability of the vorticity field in the simulations provides us with vastly greater information, which we proceed to analyse.

6.3. Coherent structures

There have been several studies on coherent structures in jet flows (Tso & Hussain 1989; Mungal & Hollingsworth 1989; Dahm & Dimotakis 1990; Yoda, Hesselink & Mungal 1994 among others). In general it is accepted that the nature of any coherent structure that may be present in jets is much less clear than in mixing layers. Fiedler (1987) estimates that while the energy in the coherent motion in mixing layers is as much as 20%, that in the far jet is only 10%. The reason may partly be that the jet is

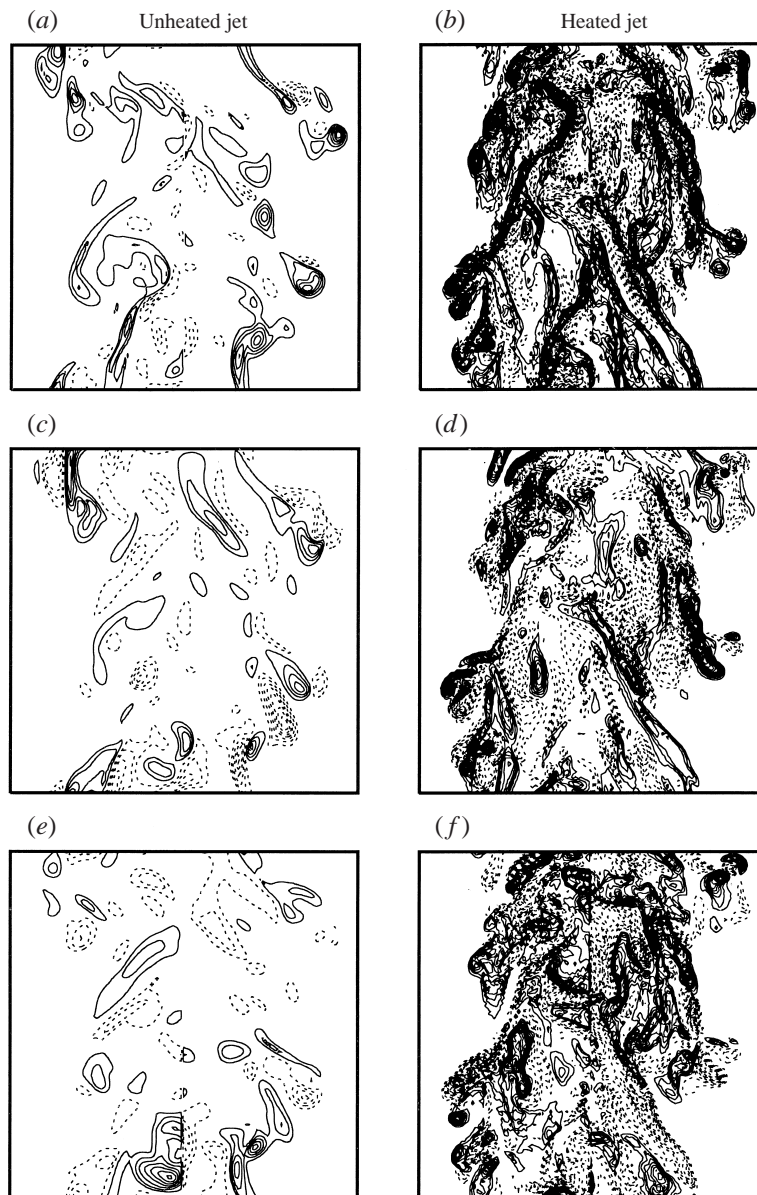


FIGURE 10. Streamwise sections (in the (y, z) -plane passing through the axis of the jet) of different components of vorticity in the unheated and heated jets at time $t = 35$. Negative contours are shown using dotted lines, starting from -0.5 in steps of -0.5 ; positive contours are shown in solid lines, in steps of 0.5 starting from 0.5 . (a, b) Azimuthal; (c, d) streamwise; (e, f) radial.

not dominated by a single instability mode: both axisymmetric and helical modes are possible, although the former is not amplified whereas the latter is. Tso & Hussain inferred, from correlation measurements, the presence of vortex rings and single and double helices: it is possible that the flow keeps switching between these modes. Dahm & Dimotakis reported, from flow visualization studies using dye in a liquid jet, that there was an ordered sequence of large arrow-head-shaped regions within which the

concentration showed little variation; while these were largely axisymmetric, there were indications of more nearly spiral modes as well.

The jet is thus both dynamically and topologically complex, as Mungal & Hollingsworth point out. It is not our objective to discuss in depth the question of coherent structures in jets in general (we shall do this elsewhere: see Siddhartha *et al.* 1999), but rather to note the effect of heating, taking advantage of the vorticity field that the present numerical simulation provides.

Now, some evidence of structures can in fact be seen in the vorticity fields already displayed. Thus, the azimuthal vorticity contours of the unheated jet, shown in figure 10(*a, b*), do suggest an arrow-head-shaped large-scale structure spanning the width of the flow, but recognition is rendered much easier if the development of the flow in time can be examined. In order to enable this, figure 11 shows the absolute magnitude of the vorticity $\|\omega\|$ in the (y, z) -plane at the late times, from $t = 25$ to $t = 35$ in steps of 2 time units. At early times, the jet is dominated by large-scale ring-like structures that show strong azimuthal instability and undergo breakdown by about $t = 20$ (not shown here). Around $t = 27$ the edge of the jet begins to be highly convoluted, and certain 'lumps' or 'structures' can be recognized. The recognition is aided if we track the structures in time, as has been done in experimental studies (Mungal & Hollingsworth 1989; Dahm & Dimotakis 1990): see in particular the regions enclosed within the sloping line boundaries in the figure, from $t = 27$ onwards. We can clearly identify structure A as it moves downstream, from its nearly central position at $t = 27$ to the top of the computational box by $t = 35$ (the computational domain being periodic, it essentially reappears from the lower side of the box as structure C). The shape and motion of this structure is not always symmetric; thus a pronounced tilt develops at its base at $t = 33$. As structure A is moving out of the box, structure B, which (in hindsight) can already be recognized at $t = 27$, moves to centre-stage around $t = 35$, while structure C is creeping up from the bottom. It is seen that while the structures A and B are not identical, they are very similar in shape: both are generally arrow-head shaped, very much like those reported in the experiments, and take about 12 time units to advect half-way down the box.

Re-examining figure 10 in the light of the above discussion, we see that the organization of the vorticity is most strongly seen in the azimuthal component ω_θ (figure 10*a*). The structure in the middle of the box here corresponds to structure B in figure 11. First, it is seen that the structure possesses a toroidal base, as ω_θ has the same sign at either end of the diameter. On top of this is a conical sheath of vorticity of the same sign. It is remarkable that there is so little azimuthal vorticity of the opposite sign anywhere within the structure. The picture that emerges is of organization of azimuthal vorticity into a thick toroidal base supporting a sheath converging to a conical tip. This is consistent with experimental results except that we do not find, at least till $t = 35$ in the unheated jet, the kind of penetration of one structure into the next that is suggested by Mungal & Hollingsworth (1989) and Yoda *et al.* (1994).

In the heated jet (also shown in figure 11), we can trace structure A as it moves up from the middle of the box towards the top end of the computational domain even after the injection of heat commences at $t = 25$. At $t = 35$ the base of the structure can be barely identified at the top. Note that such identification is possible only by tracking the trajectory of the structure; in isolation, it would be virtually impossible to do so.

Immediately following structure A is structure B, whose upper tip can already be discerned at $t = 25$. At $t = 33$ it can still be recognized, but comparison with the

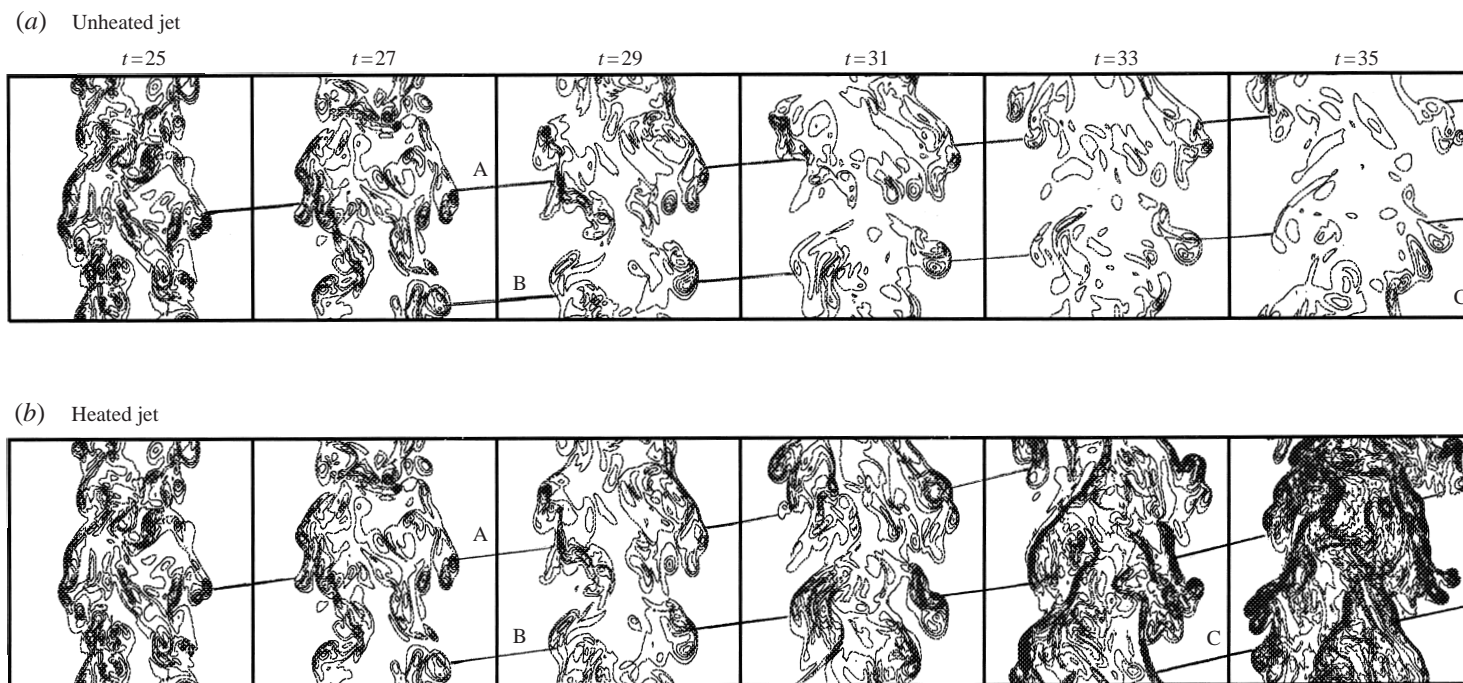


FIGURE 11. Streamwise sections (in the (y, z) -plane passing through the axis of the jet) of vorticity magnitude $\|\omega\|$ for both unheated (upper row) and heated jet (lower row) at times from $t = 25$ to $t = 35$ at intervals of 2 time units. Heat is injected between the times $t = 25$ and $t = 32$. The contour levels start from 0.5, with increments of 0.5.

corresponding panel in the unheated jet shows two major differences. (i) The vorticity magnitudes are much higher: while they decay with time in the unheated jet, they are enhanced by buoyancy in the heated jet. (ii) At $t = 35$ the structure is difficult to recognize, in particular because high values of $\|\omega\|$ occur not only towards the edges of the jet (as in the unheated case), but also in the core. At $t = 35$, structures of the kind seen in the unheated jet cannot be recognized, and high- $\|\omega\|$ regions are distributed intermittently throughout the jet – cross-stream as well as streamwise. In particular, it will be noted that the kind of large-scale ‘bulginess’ that can be seen in the unheated jet can no longer be discerned in the heated jet by $t = 35$, although smaller scale excursions are present.

Some further light is thrown on the subject by re-considering the ω_θ field previously displayed in figure 10(a,b). The field at $t = 35$ is a strong contrast to that in the unheated jet: positive azimuthal vorticity is no longer confined largely to the edges of the jet. One way of interpreting the field at $t = 35$ is that it shows that the structure B of the unheated jet has penetrated deep into structure A, introducing strong ω_θ into the core of the jet. Such penetration could occur due to the acceleration of the core that takes place when heat is injected.

In conclusion, we may say that the simulations show certain structures that, at least in overall shape and size, strongly resemble those that have been observed in the experiments. With heating, the structures persevere for some time, but by the end of the simulation they are considerably distorted, if only because acceleration due to buoyancy makes the structures telescope into each other, considerably altering whatever organization may have been present in the flow and enhancing the magnitude of vorticity. In particular, regions of very high azimuthal vorticity are now found all across the jet, rather than towards the edges of the jet as in the unheated case. Injection of heat certainly seems to reduce the large-scale bulges characteristic of the unheated jet.

More definitive statements on organized motion in the jet cannot be made at present, as the simulations provide only a very small ensemble of structures in the flow.

6.4. Enstrophy

To see quantitatively how the vorticity increases due to heating, we examine the total enstrophy, and also the enstrophies corresponding to the azimuthal, streamwise and radial components of vorticity. Computed values are shown using a linear-log scale in figure 12. In the absence of heating, the total as well as the component enstrophies all fall beyond time $t = 25$. When heat is applied, there is a virtually exponential rise of the enstrophies after some time. At $t = 35$, the enstrophies are one order of magnitude higher with heating than without. Although all three components are comparable, the azimuthal enstrophy is higher than the others by some 10%. This is consistent with equation (6.1) and the fact that $\partial\bar{T}/\partial r$ is the main contributor from the thermal field to mean vorticity generation.

6.5. Spectra

We have computed the spectra of the three vorticity components at time $t = 35$ for both the unheated and heated jets. These are shown in figure 13. The heated jet has higher energy in all modes, but the interesting thing to note is that there appears to be a preferential amplification at the higher wavenumbers. Thus, while the increase in enstrophy is about a decade at low wavenumbers, it is 3–4 decades at the highest wavenumbers. As vorticity generation depends on the temperature gradient,

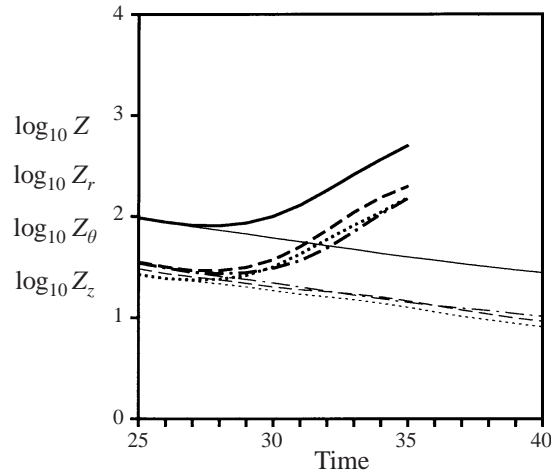


FIGURE 12. Comparison of evolution of enstrophy in the heated (shown using bold lines) and unheated (light lines) jet. Note the logarithmic scale on the y-axis. —, Z ; ·····, Z_r ; - - - -, Z_θ ; - · - · -, Z_z .

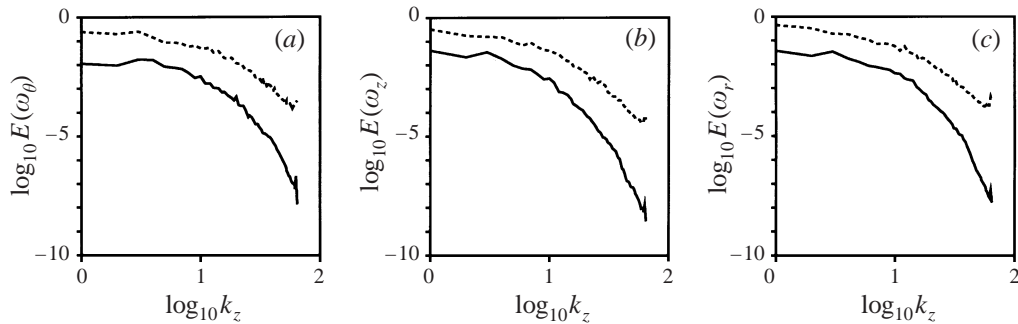


FIGURE 13. Comparison of computed spectra of different components of vorticity for the heated and unheated jets: (a) ω_θ , (b) ω_z , (c) ω_r . The spectra are plotted on log-log scales. —, Unheated jet; - - - -, Heated jet.

there is an additional weighting at the higher wavenumbers due to the derivative in the source term in (6.1). This can be clearly seen if one transforms (6.1) to Fourier space; the source term in the equation then transforms into the Fourier coefficient of temperature multiplied by wavenumber. This means that the growth rate of vorticity scales with wavenumber, thus resulting in preferential amplification of vorticity at smaller scales (higher wavenumbers).

6.6. Radial distribution of vorticity fluctuations

Figure 14 shows the radial profile of the r.m.s. vorticity fluctuations at $t = 25, 30$ and 35 , representing conditions before, during and immediately after heat injection. The large increases in vorticity fluctuations on heating are evident. However, while there is a relatively smooth rise in $\hat{\omega}'_r$ across the flow, $\hat{\omega}'_\theta$ shows a sharper peak at $r \simeq 0.7$, and $\hat{\omega}'_z$ is the sharpest of all, with the peak at $r \simeq 0.7$ to 0.9 ; it is interesting that there is such a concentration of streamwise vorticity at this location. It is presumably this peak that is responsible for the strong expulsive motions seen in the entraining velocity field (see below).

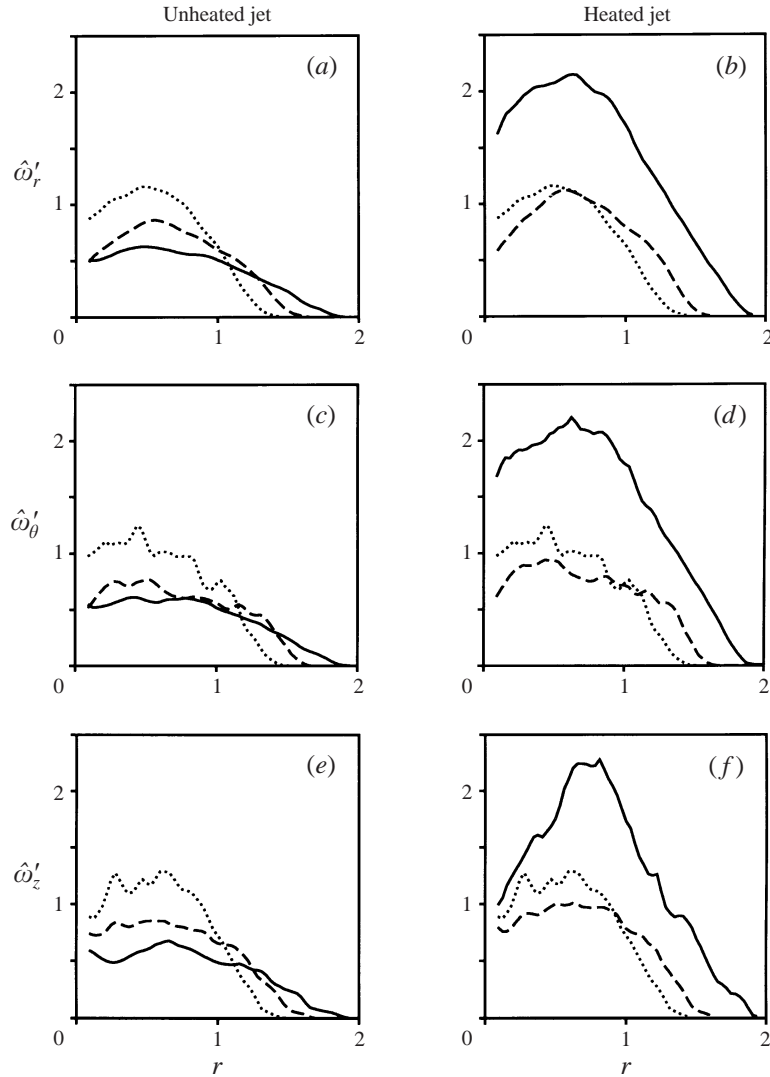


FIGURE 14. Radial distributions of $\hat{\omega}'_r$, $\hat{\omega}'_\theta$ and $\hat{\omega}'_z$ at different times for the unheated (left column) and heated (right column) jet: , $t = 25$; - - - - , $t = 30$; ———, $t = 35$.

7. The entraining velocity field

A major question concerning the development of jet flow subjected to heating is the effect on entrainment. Now because of the periodic boundary conditions imposed on the computational domain in the present simulation, the net entrainment over the domain has to vanish. Nevertheless, as we shall see below, considerable insight into the problem can be obtained by examining what we shall call the 'entraining velocity field', which displays velocity vectors in the ambient fluid in the immediate neighbourhood surrounding the jet, i.e. where the instantaneous vorticity has fallen to sufficiently low values (< 0.5).

Figure 15 shows the computed entraining velocity field at the widest transverse cross-section at $t = 35$ in the heated and unheated jets. (This corresponds to looking at the flow in the plane of a cross-section of the spatially developing jet through the

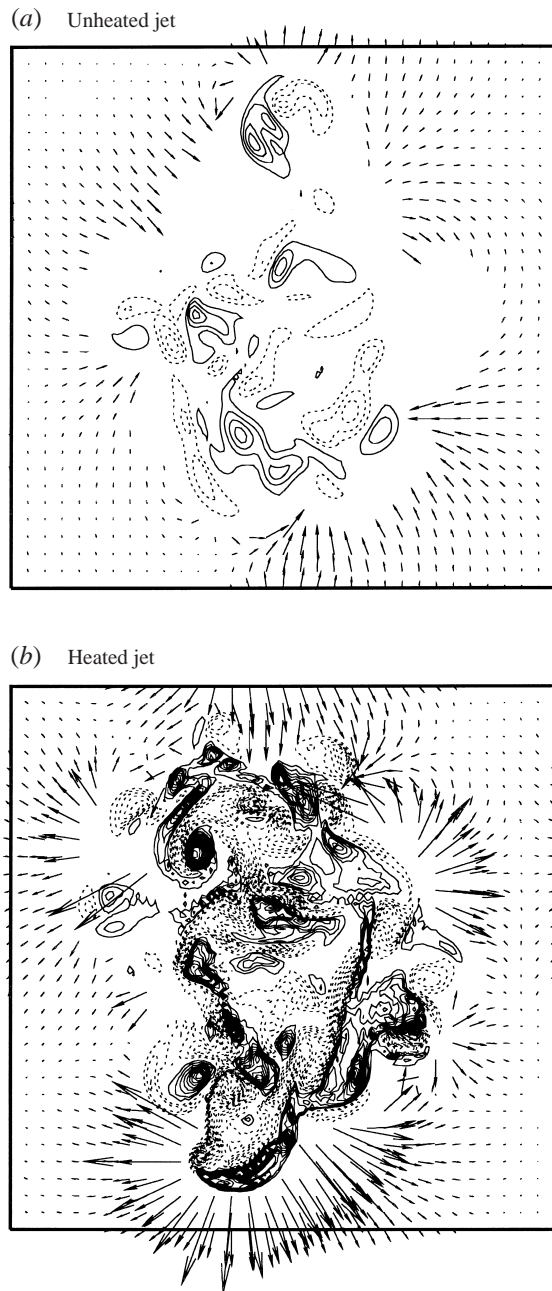


FIGURE 15. Comparison of computed entraining velocity fields at the widest transverse cross-section of the (a) unheated and (b) heated jet at time $t = 35$. The contours of streamwise vorticity, at intervals of 0.5, are shown using dotted lines for negative values and solid lines for positive values. Contour for level 0 is not shown.

base of a structure of the kind seen in figure 11.) The figure shows velocity vectors in the ambient fluid, and contours of streamwise vorticity within the jet.

The enormous increase in vorticity due to heating is once again displayed, but it will be noted that there are striking differences in the entraining velocity field in

the two cases. In the unheated case, the dominant motion is inward. The induced velocities in the heated flow are much higher. The chief difference however is that the dominant motion (certainly at the transverse section shown) now appears to be outward: there is a considerable expulsion of fluid from the vortical core of the flow. These expulsions are highly localized, and are clearly due to vorticity on a scale that is between a fifth and a tenth of the total width of the flow. The strength and direction of the motion in the horizontal plane suggests that it is due to streamwise vortex pairs. Although much more detailed analysis is required before we can be sure, we speculate that the enhancement of streamwise vorticity, due to vortex stretching and transfer from other components generated by the baroclinic torque, results in intense small-scale vortex dipoles that tend to expel core fluid into the ambient.

A word of caution is in order at this point: the scenario in figure 15(b) is typical of only certain transverse sections of the heated jet. There are obviously other stations where the mass flow across the section as a whole is inward, the present flow being constrained by periodic boundary conditions, as mentioned before. However, at no section is the inward motion found to be locally as strong as the outward motion seen at the transverse section of figure 15(b). Thus, while the net entrainment across the computational box remains zero because of the limitations of boundary conditions (it is worth noting that in this respect the simulation resembles a confined jet, where too the net entrainment must vanish because of recirculation), there appears to be a qualitative difference in the entraining velocity field near the jet between the unheated and heated cases.

In summary, we speculate that the lower entrainment observed in the experiments when heat is injected could be the consequence of two factors: the enhancement of local streamwise vorticity due to flow acceleration on heating, and a disruption and redistribution of organized azimuthal vorticity across the cross-section, for both of which the present simulations provide some support.

8. Conclusion

We have made a large number of temporal simulations of a jet that is subjected to local volumetric heating. Although a precise comparison with experiment is not possible, there is remarkable qualitative agreement between simulation and measurement on the effect of heating on the gross parameters of the flow. Thus, heating accelerates the flow and narrows the jet; absolute values of turbulence intensity increase but not as rapidly as the mean velocities, so normalized turbulence intensities are lower. It is found that the amount of heat injected, and its spatial distribution, affect the development of the flow. The strongest effects are seen for higher amount of heat injection and for narrower heating profiles.

We have shown that heating leads to dramatic increases in the vorticity and its gradients in the flow, and to striking differences in the flow characteristics. Apart from large increases in the strengths of all components of the vorticity, the coherent structure in the jet is considerably distorted and even disrupted. At the same time, due in part to vortex stretching induced by the acceleration of the flow due to buoyancy, the streamwise vortices become intense, and appear to be responsible for strong expulsive motions in the immediate ambient neighbourhood of the core flow, especially in the plane of the base of what would have been a coherent structure in the jet. On the whole, there appear to be dramatic changes in the entraining velocity field close to the jet.

This project was sponsored by ONR contract No. N00014-94-1-1133; we are grateful to Dr Gabriel Roy, ONR monitor, for his understanding support. We would also like to thank Dr G. S. Bhat and Dr Joseph Mathew of Indian Institute of Science, Bangalore, for interesting discussions, and the referees for their many useful suggestions.

REFERENCES

- BASU, A. J., NARASIMHA, R. & SINHA, U. N. 1992 Direct numerical simulation of the initial evolution of a turbulent axisymmetric wake. *Curr. Sci.* **63**, 734–740.
- BHAT, G. S. & NARASIMHA, R. 1996 A volumetrically heated jet: large-eddy structure and entrainment characteristics. *J. Fluid Mech.* **325**, 303–330.
- BROADWELL, J. E. & MUNGAL, M. G. 1991 Large-scale structures and molecular mixing. *Phys. Fluids A* **3**, 1193–1206.
- CANUTO, C., HUSSAINI, M. Y., QUARTERONI, A. & ZANG, T. 1988 *Spectral Methods in Fluid Dynamics*. Springer.
- CHEN, J. H., LIENAU, J. J. & KOLLMANN, W. 1995 Numerical simulation of low Re-number turbulence in round jets. In *Proc. Ninth Symposium on Turbulent Shear Flows*, pp. 123–145. Springer.
- CORCOS, G. M. 1988 The role of cartoons in turbulence. In *Perspectives in Fluid Mechanics* (ed. D. Coles), pp. 48–65. Springer.
- DAHM, W. J. A. & DIMOTAKIS, P. E. 1990 Mixing at large Schmidt number in the self-similar far field of turbulent jets. *J. Fluid Mech.* **217**, 299–330.
- DIMOTAKIS, P. E. 1991 Turbulent free shear layer mixing and combustion. *Prog. Astro. Aero.* **137**, 265–340.
- ELAVARASAN, R., BHAT, G. S., NARASIMHA, R. & PRABHU, A. 1995 An experimental study of a jet with local buoyancy enhancement. *Fluid Dyn. Res.* **16**, 189–202.
- FIEDLER, H. E. 1987 Coherent structures. In *Advances in Turbulence* (ed. G. Comte-Bellot & J. Mathieu), pp. 320–336. Springer.
- LIEPMANN, D. & GHARIB, M. 1992 The role of streamwise vorticity in the near-field entrainment of round jets. *J. Fluid Mech.* **245**, 643–668.
- MATHEW, J. & BASU, A. J. 1997 Reacting, circular mixing layers in transition to turbulence. Part 1: formulation, general results. *Aero. Dept. Rep. 97 FM 6*, Indian Institute of Science, Bangalore.
- MATHEW, J. & BASU, A. J. 1998 Reacting, circular mixing layers in transition to turbulence. *Phys. Fluids* (submitted).
- MCMURTRY, P. A., JOU, W.-H., RILEY, J. J. & METCALFE, R. W. 1986 Direct numerical simulations of a reacting mixing layer with chemical heat release. *AIAA J.* **24**, 962–970.
- MELANDER, M. V., HUSSAIN, F. & BASU, A. J. 1991 Breakdown of a circular jet into turbulence. In *Proc. Eighth Symp. on Turbulent Shear Flows*, pp. 15-5-1.
- MUNGAL, M. G. & HOLLINGSWORTH, D. K. 1989 Organized motion in a very high Reynolds number jet. *Phys. Fluids A* **1**, 1615–1623.
- NARASIMHA, R. 1990 The utilities and drawbacks of traditional approaches. In *Whither Turbulence? Turbulence at the crossroads* (ed. J. L. Lumley), pp. 13–48. Springer.
- NARASIMHA, R. & BASU, A. J. 1995 The effect of local volumetric heating on a turbulent jet. In *Proc. Eighth ONR Propulsion Meeting* (ed. G. D. Roy, F. A. Williams), pp. 327–333. University of California at San Diego, La Jolla CA.
- NARASIMHA, R. & SREENIVASAN, K. R. 1979 Relaminarization of fluid flows. *Adv. Appl. Mech.* **19**, 221–301.
- ORSZAG, S. A. 1971 Numerical simulation of incompressible flows within simple boundaries: I. Galerkin (spectral) representations. *Stud. Appl. Maths.* **50**, 293–327.
- RILEY, J. J., METCALFE, R. W. & ORSZAG, S. A. 1986 Direct numerical simulation of chemically reacting turbulent mixing layers. *Phys. Fluids.* **29**, 406–422.
- SIDDHARTHA, S. S., NARASIMHA, R., BASU, A. J. & KAILAS, S. V. 1999 Coherent structures in numerically simulated jets with and without off-source heating. Submitted for publication.
- TOWNSEND, A. A. 1976 *The Structure of Turbulent Shear Flow*. Cambridge University Press.
- TRITTON, D. J. 1988 *Physical Fluid Dynamics*. Clarendon Press.

- Tso, J. & Hussain, F. 1989 Organized motions in a fully developed turbulent axisymmetric jet. *J. Fluid Mech.* **203**, 425–448.
- TURNER, J. S. 1973 *Buoyancy Effects in Fluids*. Cambridge University Press.
- VENKATAKRISHNAN, L., BHAT, G. S., PRABHU, A. & NARASIMHA, R. 1998 Visualization studies of cloud-like flows. *Curr. Sci.* **74**, 597–606.
- VERZICCO, R. & ORLANDI, P. 1994 Direct simulations of the transitional regime of a circular jet. *Phys. Fluids* 1–9.
- YODA, M., HESSELINK, L. & MUNGAL, M. G. 1994 Instantaneous three-dimensional concentration measurements in the self-similar region of a round high-Schmidt-number jet. *J. Fluid Mech.* **279**, 313–350.